Experimental quantum position verification: practical challenges and single-photon correlations

Kanneworff, K.N.

5 Slow temporal demultiplexing of single photons and the normalization of two-photon correlations

To generate temporally coincident photons from a solitary single-photon source, individual photons must be extracted from a continuous stream and temporally synchronized. This process is essential for characterizing photon indistinguishability via the Hong-Ou-Mandel effect and is also relevant for applications in quantum photonics. In this work, we investigate deterministic, switch-based routing of single photons emitted by a quantum dot cavity-QED source. We focus on the regime in which the photon generation rate significantly exceeds the demultiplexing time scale and analyze the resulting long-timescale photon correlation patterns. Our measurements reveal triangular oscillations in the coincidence counts, which complicate the normalization of the second-order correlation function.

5.1 Introduction

Many quantum network and computing applications require more than one single photon, and often those photons must be mutually indistinguishable and propagate at well-defined times in individual optical modes. Traditionally, spontaneous parametric downconversion (SPDC) is used to produce heralded single photons and photon pairs [82, 83]. Since the SPDC process is inherently probabilistic this poses limits on the rate or single-photon brightness and single-photon purity of the obtained photon states [84, 85]. For the generation of *true* single photons a quantum nonlinearity is required for instance enabled by semiconductor quantum dots [84]. Recent progress with quantum-dot micro-cavity based devices has enabled high-purity sources of single photons with high brightness at excellent purity outperforming SPDC sources [60, 66, 67, 72, 75, 85, 86]. Those sources, however, produce a stream of photons in a single spatial mode, which therefore requires temporal demultiplexing into multiple spatial modes [87, 88] and their synchronization. If the single-photon source brightness is near-unity and the demultiplexing mechanism is low-loss, such demultiplexed quantum dot sources could power future optical quantum computers [57], but they also enable quantum network applications involving more than one photon [12, 17, 89]. Obviously, probabilistic beam splitter-based demultiplexing is not an option as it leads to a low success rate. Since the single-photon indistinguishability degrades with the time delay between photon production times by spectral diffusion and other decoherence mechanisms [66], fast switching (≤ 1 µs) is essential, while maintaining low-loss operation.

There are several approaches to photon switching or routing [90] that can be used for demultiplexing: Mechanical MEMS-based switching which are rather slow [91], and switches based on electro-optical modulation (EOM, [92]) either of the photon polarization or the phase, the latter in combination with Mach-Zehnder interferometers (MZI) or micro ring resonators [93]. Due to unavoidable insertion loss in integrated optics, often, free-space EOMs are used which however require high electrical drive powers and special EOM coatings to provide low-loss and high-fidelity switching [94]. Commercially, low-loss integrated-optics and fiber-coupled optical switches that operate at a suitable wavelength for InGaAs quantum dots, around 930 nm, are rather rare - in addition, since quantum dot photons are spectrally rather wide, large-bandwidth (nm range) operation is needed. Known approaches are custom integrated-optics devices [87], free-space electro-optic polarization modulation (also by the Pockels effect) and separation [88, 95–99], and integrated-optics devices [57].

We investigate an optical switch based on an EOM embedded within an MZI, with a switching time of 1 µs and an insertion loss of 0.25 dB. We focus on its application to the temporal demultiplexing of a quantum dot single-photon stream in a regime where the photon generation rate (~100 MHz) significantly exceeds the switching frequency (1 MHz). We analyze the performance of the demultiplexed photons in terms of their purity and indistinguishability, as determined through Hanbury Brown and Twiss (HBT) and Hong-Ou-Mandel (HOM) measurements. Due to the presence of triangular oscillations in the second-order correlation function, a more rigorous normalization procedure is required than is commonly used in conventional MZI-based experiments.

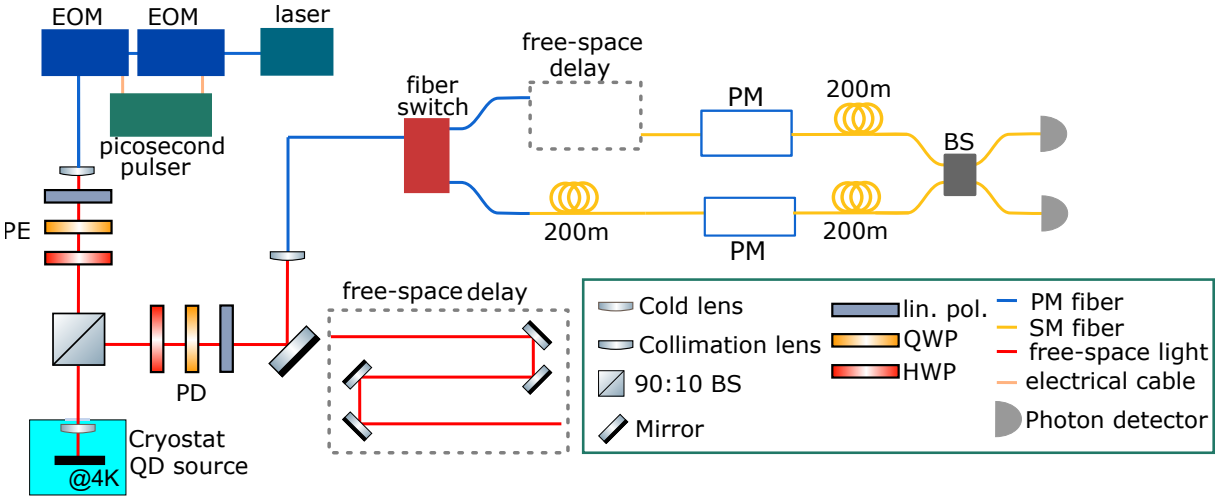

Figure 5.1: Schematic of the experimental setup. Two cascaded electro-optic modulators (EOMs) are used to generate picosecond optical pulses that excite the quantum dot source (PE and PD are polarization controllers in the excitation and detection paths). Photons are split by the fiber switch, synchronized by the 200 m fiber delay and a free-space delay line before being polarization controlled by the in-fiber polarization modulators (PM). The correlation measurements are done using a fiber-based beam splitter (BS) with two avalanche single-photon detectors.

5.2 Experimental setup

The QD is excited using short pulses [72] produced out of a narrow-linewidth frequency-tunable continuous-wave (CW) laser light using two cascaded electro-optic modulators (EOMs) controlled by custom-made electronics (see Fig. 5.1). These pulses have tunable widths and pulse period at a well-defined center wavelength. We use a single negatively charged self-assembled InGaAs/GaAs quantum dot (QD) at 4 K embedded in a micro-cavity as a single-photon source [66, 75–77]. In the device, a 31.8 nm thick tunnel barrier separates the QDs from the electron reservoir enabling quantum-confined Stark effect tuning of the QD resonance wavelength at around 935 nm [71, 77, 78]. The resonant excitation laser is filtered out using a cross-polarization method, enabling around 10^{-6} extinction [79], and the single photons are collected in a polarization maintaining (PM) single mode fiber. We use a laser power of approximately 3 nW measured in front of the window of the cryostat window.

In order to split the single-photon stream we use an optical fiber switch (Agiltron NPNS) as shown in Fig. 5.1. Because this device is relatively slow with a switching time of 1 µs, a 200 m long optical fiber is used to synchronize the sliced photon streams. We use a free-space delay line in addition to the 200 m long fiber to obtain an optical delay of exactly 1 µs, the switching time. This allows us to fine-tune the temporal wavefunction overlap of the photons at the final beam splitter.

To control the overlap of the photons in polarization space, we use two piezoelectric fiber-based polarization modulators (Polarite III PCD-M02) in each of the arms with which any arbitrary polarization state can be prepared. On each side of the interferometer arm there is an additional 200 m long 780HP single-mode fiber.

The two arms are recombined in a fiber-based beam splitter (Thorlabs TW930R5A2) and photons are detected using two single-photon avalanche detectors (SPADs, Excelitas SPCM-AQRH-14-FC-ND). We use a time-tagging card (Cronologic HPTDC, 100 ps resolution) together with custom software to obtain the two-photon correlations.

We align the temporal overlap by carefully tuning the free-space delay line. First we use short (50 ps) laser pulses in combination with faster detectors (idQuantique ID100-MMF50 SPADs, 50 ps jitter) and a different correlation card (Becker&Hickl SPC-130; start-stop correlations) for a coarse alignment, before we fine-tune the temporal overlap by optimizing HOM interference of single photons. After alignment we measure the purity of the single photons in the system by performing a Hanbury Brown and Twiss (HBT) experiment. For this, we block on arm within the free-space delay line to make sure that no two-photon HOM interference can take place. For the HOM measurement, we use both arms and tune the polarization state overlap with the polarization modulators. To characterize the polarization states in the two arms, we use continuous-wave laser light of the same frequency as used for QD excitation and measure the Stokes parameters with the use of a polarimeter (Thorlabs PAX1000IR1). This is done only before and after the correlation experiments to monitor drifts in the polarization state overlap.

5.3 Results

5.3.1 Short-time photon correlations

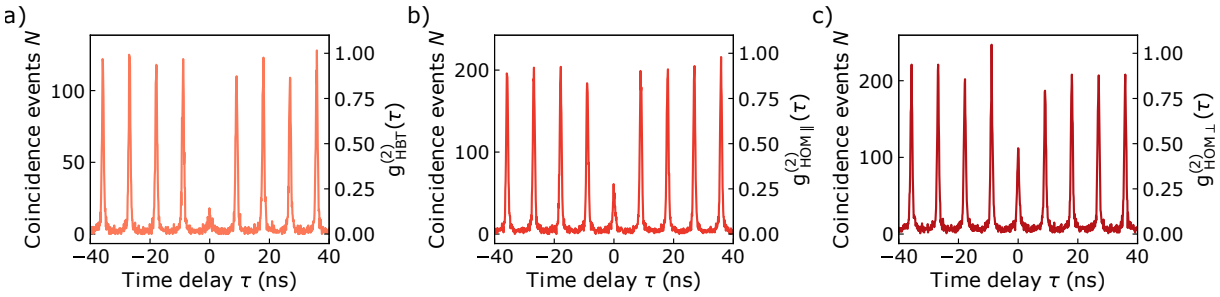

Figure 5.2: Purity and indistinguishability. With the Hanbury Brown and Twiss experiment we measure the photon purity (a), and by two-photon Hong-Ou-Mandel interference we determine the single-photon indistinguishability by comparing parallel (b) and perpendicular (c) polarization of the photons. In each figure, the left y-axis shows the raw coincidence events measured in the 5 minutes-long measurements, and the right axis shows the corresponding normalized second-order correlation function.

In Fig. 5.2 we show photon correlations measured in the HBT and HOM configuration, the latter for parallel (HOM$\parallel$) and orthogonal (HOM$\perp$) polarization of the interfering photons. The cascaded EOM pulser was set to a pulse period τ_l of 9 ns and a pulse width of 58 ps. Correlations were recorded over a time span of 5 minutes, and from this the photon coincidences were calculated up to a time delay of 200 ns, where the zero delay point was offset by 59 ns.

In order to obtain reliable values of the second order correlation function at zero-time delay $\left(g^{(2)}(0)\right)$, we determine coincidences in time-bins centered around the peaks. We

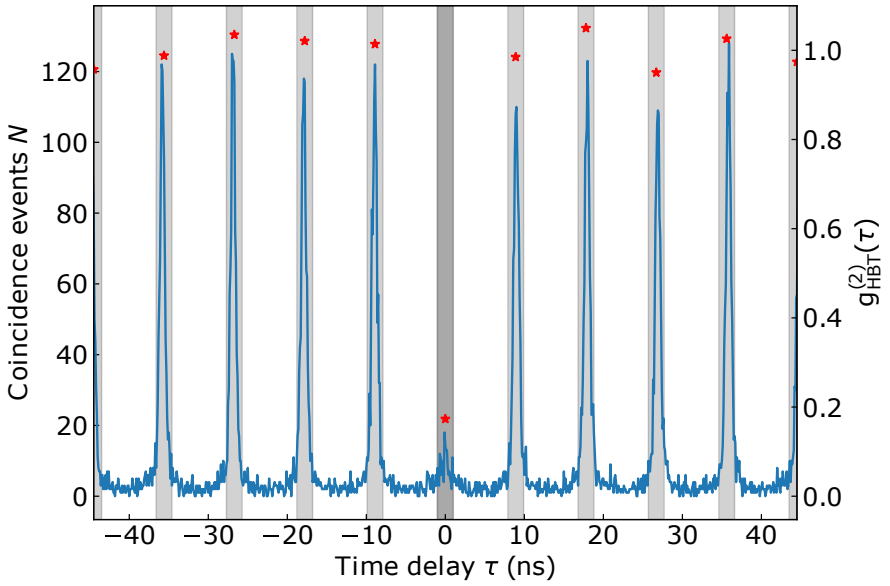

Figure 5.3: Correlation binning. To illustrate how we evaluate photon correlations, we show the HBT measurement (Fig. 5.2(a)). The gray areas show the temporal windows used to calculate the coincidence events, N_0 for the central peak at $\tau = 0$, and N_{side} for the five peaks on the left and right. The red symbols show the binned coincidence events and $g^{(2)}$ values after normalization.

determine the coincidences N_0 in the central time-bin at $\tau = 0$ as well as the averaged coincidences over the ten surrounding time-bins (five on each side of $\tau = 0$) $\bar{N}_{\text{side}}$. This allows us to normalize the coincidences and obtain $g^{(2)}(0) = N_0/\bar{N}_{\text{side}}$. An example of this normalization procedure is shown in Fig. 5.3 where the gray shaded areas indicate the 2 ns wide time bins, and the red stars the calculated $g^{(2)}$ values for each of the time bins. Table 5.1 shows the numeric results. With these numeric results we can also give a value of both the HOM interferometric visibility (Eq. 5.1) and the indistinguishability (Eq. 5.2) of the single-photon source [62, 100], resulting in $\mathcal{V}_{\text{HOM}} = 0.456 \pm 0.028$ and $M_{\text{simple}} = 0.535 \pm 0.054$.

$$\mathcal{V}_{\text{HOM}} = \frac{g^{(2)}_{\text{HOM}\perp}(0) - g^{(2)}_{\text{HOM}\parallel}(0)}{g^{(2)}_{\text{HOM}\perp}(0)} \tag{5.1}$$

$$M_{\text{simple}} = \mathcal{V}_{\text{HOM}} \left(1 - g^{(2)}_{\text{HBT}}(0)\right) \tag{5.2}$$

Equation 5.2 is the simplified version assuming a perfect interferometer. In the previous chapter of this thesis we have shown this not to be always true and we have developed an extended model including experimental imperfections resulting in equation 5.3 below. The description that is derived for a Mach-Zehnder interferometer also applies to the temporal demultiplexing system here, since the switching time is significantly larger than the pulse period of the quantum dot excitation laser. The treatment of R_1 and T_1, the reflection and transmission coefficients of what in the MZI system would be the first beam splitter, is slightly different. For the optical switch, these coefficients correspond

	N_0	$\bar{N}_{side}$	$g^{(2)}(0)$
HBT	174±13	1004±32	0.173±0.014
HOM ∥	573±24	1738±42	0.330±0.016
HOM ⊥	1097±33	1807.3±46	0.607±0.023

Table 5.1: Raw coincidences and second-order correlation function values with corresponding statistical errors, of the measured data shown in Fig. 5.2. N_0 are the counts in the central time-bin, $\bar{N}_{side}$ the averaged counts of the 10 nearest bins (five on each side of $\tau = 0$). $g^{(2)}(0)$ is obtained after normalization.

to the transmissions towards either output (T_1 is towards the top output in Fig. 5.1), and therefore it no longer holds that $R_1 + T_1 = 1$. Coefficients R_2 and T_2 still describe the reflection and transmission coefficients of the final beam splitter (BS in Fig. 5.1). η_s and η_l are the transmissions through the arms of the interferometer and $V_{p\|}$ and $V_{p\perp}$ are the average polarization state overlap measured for the HOM∥ and HOM⊥ correlation measurements. The values of all experimental parameters are given in Appendix 5.5.1 and we obtain an indistinguishability $M_{\text{full}} = 0.545$. Since this is very close to M_{simple} and the difference between $\mathcal{V}_{\text{HOM}}$ and M_{simple} is larger, we can conclude that the purity of the single-photon source is more influencing the indistinguishability than the experimental imperfections.

$$M_{\text{full}} = \frac{\mathcal{V}_{\text{HOM}}\left[T_1\eta_s R_1\eta_l\left(T_2^2+R_2^2\right)+g^{(2)}_{\text{HBT}}(0)R_2T_2\left(T_1^2\eta_s^2+R_1^2\eta_l^2\right)\right]}{2T_1\eta_s R_1\eta_l R_2T_2\left[V_{p\|}-V_{p\perp}\left(1-\mathcal{V}_{\text{HOM}}\right)\right]} \tag{5.3}$$

5

5.3.2 Long-time photon correlations

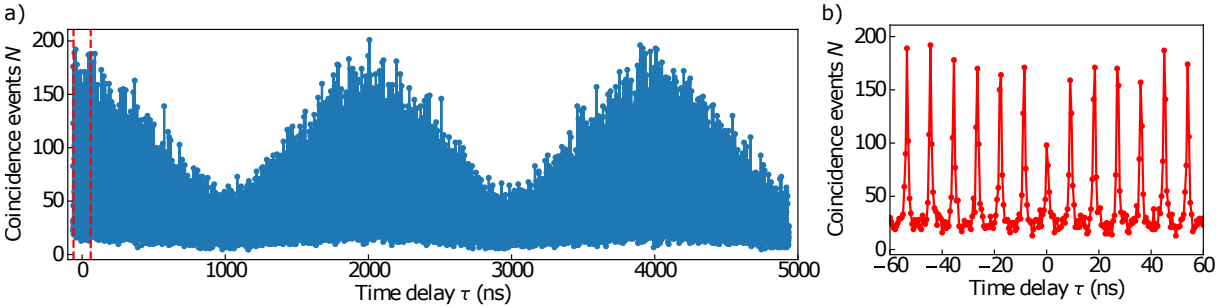

Figure 5.4: Long-time HOM correlations for the switch experiment with a switching time of 1 µs and synchronization. Coincidences are calculated for a time delay of up to 5 µs (a); panel (b) shows a magnification of the region in (a) indicated by dashed lines.

Because the optical switching is much slower than the excitation of the quantum dot, we need to look at a longer time window to see the effect of the switch on the HOM photon correlations. The result is shown in Fig. 5.4(a), which shows correlations with a detection

delay of up to 5 µs with undetermined polarization state overlap. This long time delay is possible by the time-tagging approach and our custom analysis software. The reduced peak at zero time delay appears to be absent, but this is only due to the enormous amount of data, as the correlations measured at zero time delay are clearly visible in the magnified view in Fig. 5.4(b). Furthermore, we observe triangular oscillations of the coincidence peak heights, and to a lesser degree also of the background coincidences between the peaks.

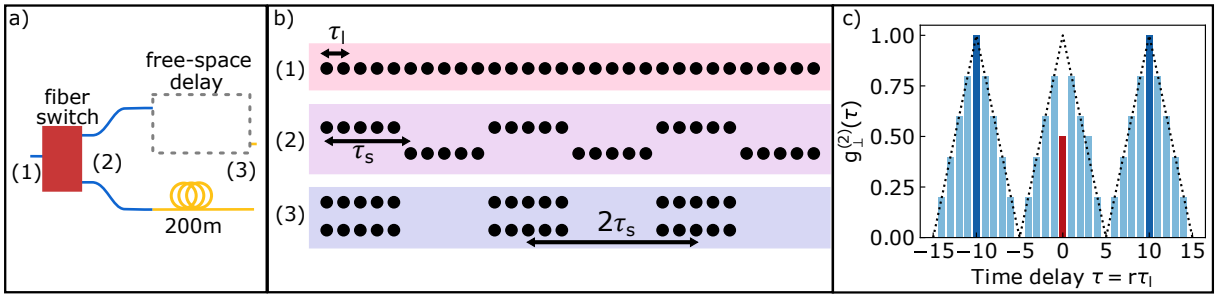

Figure 5.5: Illustration of temporal demultiplexing. We assume that the demultiplexing occurs in bunches of five photons, i.e., the switching time τ_s is five times larger than the time between two consecutive photons τ_l. Schematic representation of the demultiplexing part of the setup (a). Panel (b) shows schematically the single-photon streams before the switch (1), after the switch but before the temporal delay (2) and after the temporal delay (3). The simulated photon correlations assume triangular shape (c), where the dotted lines emphasize the shape of the triangular oscillations that arises.

In order to get a deeper understanding, we now develop a simple model of the temporal demultiplexing experiment which is illustrated in Fig. 5.5(a). We assume the switch to be slow meaning that the switching time τ_s is longer than the time between two consecutive photons in the single-photon stream (or pulse period) τ_l; and for this particular example we assume $\tau_s = 5\tau_l$. Before the switch [(1) in Fig. 5.5(b)] there is a single long stream of photons, and the switch outputs are then routed to the two paths in bunches of five (2). The temporal delay then synchronizes both photon streams (3). This leaves empty time bins, in this example five, followed by five occupied time bins in both streams. This means that during one period and for a time delay $\pm\tau_s$ there is no combination of photons that can result in a coincidence event, while for a time delay of $\pm 2\tau_s$, there are five possibilities, with linear interpolation in between. Hence, the second order correlation function assumes a triangular shape as shown in Fig. 5.5(c). In general, ignoring HOM interference at $\tau = 0$, we obtain zero coincidence events at odd multiples of the switching time, and maximal correlations at even multiples of the switching time. The slope of the resulting triangular oscillations depends on τ_l/τ_s, the ratio between the time delay between two consecutive photons and the switching time. If τ_s is only slightly larger than τ_l, as discussed in this particular example where $\tau_s = 5\tau_l$, the correlations at time delay $\pm\tau_l$ deviate strongly from the maximum correlations (by 20% in Fig. 5.5(c)). If one would use the "standard" method of normalization described earlier it would result in a gross overestimation of $g^{(2)}(0)$ and consequently in wrong purity and indistinguishability values. Therefore, the normalization of experimental data needs to be done carefully, and in principle, only the correlations at even multiples of the switching time should be used.

If, however, like in our case where the switch is much slower than the time between two consecutive photons ($\tau_s \gg \tau_l$), using correlations for normalization around $\tau = 0$ leads to relatively small error, due to slope being shallow in this case.

For instance, in our long-time correlation experiment with $\tau_s = 1$ µs and $\tau_l = 9$ ns, there are approximately 111 peaks underneath one half of the triangular shape, and for normalization we have used the first five side-peaks as shown in Fig. 5.5(c). The difference in $g^{(2)}$ value between two consecutive peaks is theoretically around ≈ 0.009, which results in an averaged peak height of 0.973 instead of 1.0, adding 3 % error to $g^{(2)}$. To confirm this claim we tested both the method displayed in Fig. 5.3, henceforth named the "nearby normalization", and the method where only correlations corresponding to a multiple of the switching time τ_s are used for normalization, to which we will refer to as the "exact normalization", on the long time delay data from Fig. 5.4. For both methods time bins of 3 ns were used. The values of the coincidences in the central time bin N_0, the average coincidences in the time bins used for normalization $\bar{N}_{side}$ and the resulting correlations at zero time delay $g^{(2)}(0)$ are shown in table 5.2. The value of N_0 is naturally independent of the method, since the method only affects which surrounding bins are used for the normalization, hence only affecting $\bar{N}_{side}$. The resulting $g^{(2)}(0)$ extracted with the exact normalization is smaller by 0.03 compared to the $g^{(2)}(0)$ calculated with the nearby normalization. This corresponds to a difference of 4 % which is comparable to the expected error of 3 %.

Normalization:	nearby	exact
N_0	383±20	
$\bar{N}_{side}$	542±23	566±24
$g^{(2)}(0)$	0.71±0.05	0.68±0.05

Table 5.2: Model comparison. Coincidences in the central time bin N_0, the average coincidences in the time bins used for normalization $\bar{N}_{side}$ and the resulting correlations at zero time delay $g^{(2)}(0)$ comparing the "nearby normalization" and "exact normalization" method applied to the long time delay coincidences shown in Fig. 5.4.

Finally, we observe in Fig. 5.4(a) that the offset also oscillates synchronously with the peak height. The offset is more clearly visualized in Fig. 5.4(b) and is caused by a multi-photon component mostly caused by imperfect extinction of the excitation laser. These unwanted photons are also routed to the two paths and the same arguments hold as explained for the single photons, therefore the offset oscillation is expected. The apparent rounding of the triangular oscillations is mostly likely caused by the shot noise in the measurement.

5.4 Conclusions and outlook

We have investigated how temporal demultiplexing influences the second order correlation function and found that normalization has to be done carefully. In a Hong-Ou-Mandel experiment with an optical switch with a switching time τ_s =1 µs that is much larger than the pulse period of the excitation laser $\tau_l = 9$ ns, we have measured two-photon correlations over a period of approximately 5 µs. The correlations show triangular oscillations, which are well explained by a simple model. We find that even in the case of $\tau_s \gg \tau_l$, the normalization error for $g^{(2)}(0)$ can be on the order of a few percent but can be mitigated easily if the oscillations are taken into account.

5.5 Appendix

5.5.1 Experimental parameters

Table 5.3 shows an overview of all required experimental parameters to calculate the indistinguishability M taking account of all imperfections in the interferometer. Unlike a standard MZI system here R_1 and T_1 are the transmission coefficients of the optical fiber switch when either 0 V or 1.4 V is applied and therefore do not add up to 1.

	Temporal demultiplexer
$g^{(2)}(0)$	0.173±0.014
$g^{(2)}_{\parallel}(0)$	0.330±0.016
$g^{(2)}_{\perp}(0)$	0.607±0.023
$\mathcal{V}_{\mathrm{HOM}}$	0.456±0.028
$V_{p\parallel}$	0.9971
$V_{p\perp}$	0.0019
R_1	0.60
T_1	0.71
η_l	0.70
η_s	0.67
R_2	0.54
T_2	0.46

Table 5.3: Experimental parameters.